Constraining Properties of Dark Matter particles Using Astrophysical Data

Iakubovskyi, D.

Chapter 2

Mass of the dark matter particles

2.1 Introduction

In this Chapter we discuss the lower bounds on the mass of dark matter particles, coming from the analysis of dark matter phase-space distribution in different types of dark matter dominated objects.

If the dark matter particles are fermions, there is a very robust bound on their mass. Namely, due to the Pauli exclusion principle, there exists the densest "packing" of the fermions in a given region of the phase space [45]. Decreasing the mass of dark matter particles, one increases their number in a given gravitationally bound object, containing dark matter. The requirement that the phase-space density of the dark matter does not exceed that of the degenerate Fermi gas leads to the *lower mass bound*. A weaker version of the same bound can be generalized for the bosonic dark matter as well. We review the existing approaches, and concentrate on two methods of deriving such a bound. The first (model-independent) approach uses the information about the *observed* matter distribution only and applies to any type of fermionic dark matter. The second method also requires an assumption about the initial (primordial) distributions of dark matter velocities. Stronger, model-dependent bounds are quoted for several dark matter models (thermal relics, non-resonantly and resonantly produced sterile neutrinos, etc.). These latter bounds rely on the assumption that baryonic feedback cannot significantly increase the maximum of a distribution function of dark matter particles. It turns out that the strongest bound comes from the objects with the largest phase-space density – dwarf spheroidal galaxies (dSphs). We discuss the ob-

servational data on dSphs as well as astronomical uncertainties in relevant parameters.

While these considerations are very generic and rely almost exclusively on such fundamental properties of dynamical systems like Liouville theorem, they provide important restrictions on possible particle physics models. For example, applying these considerations to the case of neutrino dark matter would rule out the possibility that massive neutrinos constitute the dominant fraction of dark matter in the Universe (the lower bound of their mass would imply that the $\Omega_{\rm DM} \ll 1$). For the scenario in which all the dark matter is made of sterile neutrinos produced via non-resonant mixing with the active neutrinos (NRP) this gives $m_{\rm NRP} > 1.7 \text{ keV}/c^2$. Combining these results in their most conservative form with the X-ray bounds of dark matter decay lines, we conclude that the non-resonant production scenario remains allowed in a very narrow parameter window only. This conclusion is independent of the results of the Lyman-α analysis. The dark matter model in which sterile neutrinos are resonantly produced in the presence of lepton asymmetry remains viable. Within the minimal neutrino extension of the Standard Model (the νMSM), both mass and the mixing angle of the dark matter sterile neutrino are bounded from above and below, which suggests the possibility for its experimental search.

This Chapter is organized as follows. After an overview of the original Tremaine-Gunn bound and its modifications (Section 2.2), we introduce the concept of maximal coarse-graining and propose a conservative modification of the original bound (Section 2.3). In Section 2.4 we analyze existing observational data on Milky Way and Andromeda galaxies, galaxy groups and Milky Way satellite dSphs and use it to determine the phase-space density of these objects. Special attention is paid to systematic uncertainties of measured values. Our results are summarized in Section 2.6.

2.2 Dark matter mass limits

Consider a spherically symmetric dark matter-dominated object with the mass M within the region R. One can obtain the lower bound $m_{\rm DEG}$ on the dark matter mass by demanding that the maximal (Fermi) velocity of the degenerate fermionic gravitating gas of mass M in the volume $\frac{4}{3}\pi R^3$ does

not exceed the escape velocity $v_\infty = \left(\frac{2G_N M}{R}\right)^{1/2}$:

$$\hbar \left(\frac{9\pi M}{2g m_{\rm DEG}^4 R^3}\right)^{1/3} \leq \sqrt{\frac{2G_N M}{R}} \Rightarrow m_{\rm DEG}^4 \geq \frac{9\pi\hbar^3}{4\sqrt{2} g M^{1/2} R^{3/2} G_N^{3/2}}. \qquad (2.1)$$

Here and below g denotes the number of internal degrees of freedom of dark matter particles, and G_N is the Newton's constant. Such a consideration, applied to various dark matter dominated objects, leads to the mass bound, which we will call $m_{\rm DEG}$ in what follows (see Table 2.4 below).[1]

The above considerations assume that the dSphs are *purely spherical* systems. Analysis of [166] shows that ellipticity of stars in dSphs vary from $0.22^{+0.18}_{-0.22}$ for Leo IV to 0.80 ± 0.04 for Ursa Major I. Simulated dark matter halos on the other hand tend to have rather moderate ellipticity, $\epsilon_{\rm DM} \lesssim 0.32$ [167].[2] According to Section 2.5, the ellipticity of dark matter halos can lower the resulting limit on $m_{\rm DEG}$ by $\lesssim 10\%$.

The limit, obtained in such a way, is very robust, as it is independent of the details of the formation history of the system. The only uncertainties associated with it are those of astronomical nature: systematic errors in the determination of velocity and density distribution. All these issues will be discussed below (Section 2.4, 2.3).

For particular dark matter models (with the known primordial velocity dispersion) and under certain assumptions about the evolution of the system which led to the observed final state, this limit can be strengthened [45, 46, 48, 49, 157, 168–173]. The argument is based on the *Liouville's theorem* (see e.g. [168, 174]) and assumes that the collapse of the system is disipationless and collisionless. The Liouville theorem states that the phase-space distribution function $f(t, x, v)$ does not change in the course of disipationless collisionless dynamics. The consequence of the Liouville theorem is that the function $f(t, x, v)$ "moves" in the phase-space, according to the Hamiltonian flow, and therefore its maximum (over the phase space) remains unchanged. Therefore, if one could determine the characteristics of a phase-space distribution function from astronomically observed quantities (in the first place

[1] The spatially homogeneous dark matter distribution is only an approximation. In reality one should consider self-gravitating degenerate fermionic gas. It is possible to show that, under some external conditions, the system of weakly interating fermions undergoes a first-orger phase transition to a nearly degenerate "fermion star" [164]. The existence of such objects may also have insteresting astrophysical applications [165].

[2] Therefore it is hard to explain the ellipticity of stars in the most elongated dSphs, see the discussion in [166].

average density $\bar{\rho}$ and velocity dispersion σ) in dSphs (or any other dark matter dominated objects), the Liouville theorem would allow to connect the measured values with the primordial properties of dark matter particles.

One such characteristics of the phase-space distribution is its *maximum*. Any physical measurement can probe only the phase-space distribution, averaged over some phase-space region – a *coarse-grained* phase-space density (phase-space density) (as opposed to exact or *fine-grained* phase-space density). Such a coarse-grained phase-space density, averaged over phase-space cells $\Delta\Pi(x,v)$ centered around points (x,v) in the phase space, is defined via

$$\bar{f}(t,x,v) = \frac{1}{\mathrm{vol}(\Delta\Pi)} \int\limits_{\Delta\Pi(x,v)} d\Pi'\, f(t,x',v') \tag{2.2}$$

(here $\mathrm{vol}(\Delta\Pi)$ is the volume of the phase-space cell). From the definition (2.2) it is clear that the maximal (over the whole phase space) value of the coarse-grained phase-space density $\bar{f}_{max}(t)$ cannot exceed the maximal value of the corresponding fine-grained phase-space density. On the other hand, as a consequence of the Liouville theorem, the maximum of the fine-grained phase-space density f_{max} does not change in time. Thus, one arrives to the following inequality

$$\bar{f}_{max}(t) \leq f_{max}\ . \tag{2.3}$$

The inequality (2.3) allows to relate the properties of dark matter at present time t with its primordial properties, encoded in f_{max}. For example, if one assumes that initially dark matter particles possess relativistic Fermi-Dirac distribution function with some temperature $T_{\rm FD}$ (relativistically decoupled thermal relics):

$$f_{\rm FD}(p) = \frac{g}{(2\pi\hbar)^3} \frac{1}{e^{p/T_{\rm FD}}+1} \tag{2.4}$$

and recovers from astronomical measurements that in the final state the coarse-grained phase-space density of the system is described by the isothermal sphere (see e.g. [174]) with a core radius r_c and a 1D velocity dispersion σ, whose maximum is given by

$$\bar{f}_{iso,max} = \frac{9\sigma^2}{4\pi G_N (2\pi\sigma^2)^{3/2} r_c^2} \tag{2.5}$$

the comparison of the maximum of the coarse-grained phase-space density (2.5) with its primordial (fine-grained) value leads to the so-called Tremaine-

Gunn mass bound [45]:

$$m_{\rm FD} \geq m_{\rm TG}, \quad \text{where} \quad m^4_{\rm TG} \equiv \frac{9(2\pi\hbar)^3}{(2\pi)^{5/2} g G_N \sigma\, r_c^2}. \tag{2.6}$$

For the case of initial distribution (2.4) this bound is stronger than the one, based on the Pauli exclusion principle, by a factor $2^{1/4}$ [45]. For different primordial dark matter distributions this difference can be significant (as we demonstrate later). We would like to stress, though, that these stronger bounds make assumptions about the evolution of phase-space density, while the one, based on the Pauli exclusion principle does not assume anything about either primordial velocity distribution of the particles, or the formation history of the observed object and simply compares measured phase-space density with the maximally allowed for fermions.

Another characteristics of the phase-space distribution function is the "average phase-space density"

$$Q \equiv \frac{\bar{\rho}}{\langle v^2 \rangle^{3/2}}\ , \tag{2.7}$$

introduced in [175, 176]. The value of Q_f (average phase-space density today) is simply defined in terms of the observed quantities $\bar{\rho}$ and $\langle v^2 \rangle = 3\sigma^2$ and therefore serves as a convenient estimator of the phase-space density for any dark matter dominated object. One can calculate primordial Q_i for an arbitrary homogeneous distribution function $f(p)$

$$Q_i = \frac{g\, m^4}{(2\pi\hbar)^3} \frac{\left(\int f(p) d^3p\right)^{5/2}}{\left(\int f(p) p^2 d^3p\right)^{3/2}} \tag{2.8}$$

and compare it with its value today Q_f. It was claimed in [175, 176] that Q cannot increase during the evolution of dark matter:

$$Q_i \geq Q_f. \tag{2.9}$$

Applying this inequality to the dSphs, one obtains several times stronger mass bound, than that of [45].

To illustrate the origin of the inequality (2.9), authors of [175, 176] noticed that in the case of the *uniform monoatomic ideal gas*, Q is related to the usual thermodynamic entropy per particle (see Appendix 8.2.1.1) and the

inequality for Q becomes a consequence of the second law of thermodynamics. Indeed, in this case one can see that

$$\frac{S[f]}{N} = -\log\left(\frac{Q(\bar{\rho},\sigma)\hbar^3}{m^4}\right) + \log C[f]\ , \tag{2.10}$$

where in the right hand side of (2.10) functional $C[f]$ does not depend on the average density and velocity of the dark matter particles.

However, because of the long-range interaction of dark matter particles, the notion of Boltzmann entropy is well-defined only for the primordial dark matter distribution and not for the final state of dark matter evolution (see e.g. the discussion in [177]). Moreover, we will show below that in general *the increase of entropy does not imply the decrease of* Q. Indeed, the values of $C[f]$ are different for different types of phase-space distributions f and therefore they can change with time if the shape of the (coarse-grained) distribution changes. Namely, even if initial (i) and final (f) states both satisfy relation (2.10) between the entropy and Q ($S_{i,f} = \log C_{i,f} - \log \frac{Q_{i,f}\hbar^3}{m_{\rm DM}^4}$) from the second law of thermodynamics

$$S_f \geq S_i \tag{2.11}$$

it only follows that

$$Q_i \geq Q_f \frac{C_i}{C_f}\ . \tag{2.12}$$

Therefore, in general, the inequality (2.9) does not follow from entropic considerations.

Moreover, the simple relation (2.10) between the entropy and Q does not hold for the distributions we are interested in. For example, for the Fermi-Dirac distribution (2.4) one has:

$$\frac{S}{N} = \text{const}\frac{m_{\rm FD}^4}{Q\hbar^3} \tag{2.13}$$

(see Appendix 8.2.1.3 for details). The relation becomes even more complicated, if one considers dark matter candidates (e.g., sterile neutrinos, gravitinos), which are produced out of thermal equilibrium. In general, when the primordial distribution function depends on several parameters, both Q and entropy are expressed through these parameters in a non-trivial way and the simple relation (2.10) does not hold. For example, this is the case when dark matter is produces in two stages and the dark matter distribution

shape has two components: colder and warmer one. Physically interesting examples include: production of sterile neutrino in the presence of lepton asymmetry [78, 87, 88]; production of gravitino thermally at high temperatures (see e.g. [178, 179]) accompanied by non-thermal production via late decays of next-to-lightest supersymmetric particles (see e.g. [180]).

Keeping in mind the above considerations, one might be tempted to use the entropy of the system as an estimator of phase-space density and utilize the entropy increase (2.11) instead of the inequality on Q to put a lower bound on the dark matter mass. However, unlike Q, which by definition is expressed solely in terms of measured quantities $\bar{\rho}$ and σ, the inequality (2.11) requires the knowledge of the phase-space distribution function in the final state (e.g. to determine the C_f in the right-hand side of Eq. (2.10) or, more generally to express the entropy of the final state in terms of the observed quantities). This information cannot be simply deduced from astronomical observations. One possible way to formulate a conservative, robust inequality would be to find the *maximal* possible entropy for a given system with measured macroscopic parameters. However, it was shown in [168, 174, 181, 182] that such a maximum does not exist. Namely, for a gravitating system which usually consists of a compact core and a widely dispersed halo of finite mass, the total Boltzmann entropy of the system goes to infinity when the halo becomes infinite. Physically, the measured density and velocity dispersion characterize the inner part of the object. The astronomical observations do not usually probe the outskirts of gravitating systems (such as dSphs) and phase-space distributions (such as (2.5)) do not describe them properly. On the other hand, to compare with the homogenous initial system having a primordial velocity spectrum, we need to know an entropy of the *whole* system. The large (and unknown!) fraction of this entropy can be related to the outskirts. The entropy of the gravitating system depends on the precise state of the halo.

As a result, *it is not possible to construct a simple and robust limit, using entropy considerations*.

2.3 Maximal coarse-graining

In view of the above arguments, to derive a conservative mass bound, in this work we will follow the original approach of Tremaine and Gunn [45] with

some modification.

An important advantage of this approach is that the maximum of the phase space density is likely to be located in the inner, dense part of an object. Therefore, under this reasonable assumption, the results *do not depend* on the dark matter distribution in the outskirts (see the discussion above).

As discussed already, the coarse-grained phase-space distribution in the final state cannot be measured directly, and one has to make assumptions to deduce its maximum. A conservative way to minimize this uncertainty is to use the "maximally coarse-grained distribution". It is based on a simple fact that the mean value of a function, averaged over an arbitrary region cannot exceed its maximal value. Therefore, the average value of coarse-grained phase space density in a large phase-space volume can be taken as a conservative estimate of the $\bar{F}_{max}$, independent on assumptions about the actual form of phase-space distribution.

To this end we consider an (approximately spherically symmetric) gravitating system (having in mind a dwarf spheroidal galaxy), that has the mass $M(R)$ confined within the radius R. The phase-space volume, occupied by the dark matter particles, forming such a system can be approximated by

$$\Pi_\infty = \left(\frac{4}{3}\pi\right)^2 R^3 v_\infty^3 \ , \tag{2.14}$$

where we have introduced *escape velocity* v_∞. The "coarsest" phase-space density is such that the averaging (2.2) goes over the whole phase-space volume: $\Delta\Pi = \Pi_\infty$:

$$\bar{F} = \frac{M}{\Pi_\infty} = \frac{9}{16\pi^2}\frac{M}{R^3 v_\infty^3} = \frac{3\bar{\rho}}{4\pi v_\infty^3} \tag{2.15}$$

As an estimate for R we take *half-light radius* r_h (i.e. the radius where surface brightness profile falls to 1/2 of its maximal value). Neglecting possible influence of ellipticity of stellar orbits (c.f. Section 2.5), assuming constant dark matter density within r_h and isothermal distribution of stars [183], we obtain the following estimate on the average dark matter density within r_h:

$$\bar{\rho} = \frac{3\log 2}{2\pi}\frac{\sigma^2}{G_N r_h^2}, \tag{2.16}$$

Assuming isotropic velocity distributions,[3] the escape velocity v_∞ of the dark matter particles is related to the velocity dispersion σ via $v_\infty \simeq \sqrt{6}\sigma$. In such

[3]This assumption seems to be correct for the dark matter particles, since numerical simu-

a way we obtain the averaged phase-space density $\bar{F}$:

$$\bar{F} = \frac{M}{\Pi_\infty} = \frac{\bar{\rho}}{8\pi\sqrt{6}\sigma^3} \approx \frac{3\log 2}{16\sqrt{6}\pi^2 G_N \sigma r_h^2} \approx \tag{2.17}$$
$$\approx 1.25\,\frac{M_\odot}{\mathrm{pc}^3}\left(\frac{\mathrm{km}}{\mathrm{sec}}\right)^{-3}\left(\frac{\mathrm{km/sec}}{\sigma}\right)\left(\frac{1\,\mathrm{pc}}{r_h}\right)^2 ,$$

which coincides with its maximal value (being flat).

As a consequence of Eq. (2.3), this "coarse-grained" phase-space density $\bar{F}$ is smaller than the f_{max} – the maximum value of fine-grained phase-space density, equal to its primordial value:

$$\bar{F} \leq f_{max} \ . \tag{2.18}$$

Eq. (2.18) relates the observed properties of the dark matter-dominated systems (l.h.s.) with the microscopic quantity on the r.h.s. of inequality, which depends on the production mechanism of the dark matter.

We are mostly interested in two types of primordial momentum distribution. One is the relativistic Fermi-Dirac (2.4) with its f_{max} being equal to

$$f_{max,\mathrm{FD}} = \frac{g\, m_{\mathrm{FD}}^4}{2(2\pi\hbar)^3} \tag{2.19}$$

(we fix the overall normalization of the phase-space distribution function by the relation $M = \int d^3x\, d^3v\, f(t,x,v)$, where M is the total mass of the system). Another one is an (approximate) form of the momentum distribution for sterile neutrinos, produced via non-resonant oscillations with the active ones [56, 73]. For the latter case we consider the velocity dispersion to be[4]

$$f_{\mathrm{NRP}}(p) = \frac{g\chi}{e^{p/T_\nu}+1} \ . \tag{2.20}$$

lations of dark matter structures of different scales show that the velocity anisotropy $\beta(r) \equiv 1 - \frac{\sigma_\theta^2+\sigma_\phi^2}{2\sigma_r^2}$ tends to be zero towards the central region [184–188]. It is not clear whether β equals to zero for stars in dSphs. The assumption of isotropy of stellar velocities leads to the *cored* density profiles [189, 190], therefore our estimate for $\bar{\rho}$ tends to be robust. This is confirmed by comparison of the estimate (2.16) with those, based on [191–193], where dark matter density profiles were obtained under the assumptions of different anisotropic distributions of stars in dSphs.

[4]In reality the momentum distribution in the case of non-resonant production does not have thermal shape. The exact shape, taking into account contributions from primeval plasma at temperatures around QCD transition, can be computed only numerically [81, 86]. The difference between the exact distribution and (2.20) does not exceed 20%, which does not affect the mass bounds.

The normalization constant χ is proportional to the mixing strength between active and sterile neutrinos and T_ν is the temperature of neutrino background $T_\nu(z) = (1+z)T_{\nu_0}$, related to the temperature of the cosmic microwave background today via $T_{\nu_0} = (4/11)^{1/3} T_{\rm CMB,0}$. For the maximal value of distribution (2.20) we find

$$f_{max,\rm NRP} = \frac{g\chi m_{\rm NRP}^4}{2(2\pi\hbar)^3}\,. \tag{2.21}$$

From the definition (2.20) one can relate the normalization factor $g\,\chi$ to the dark matter abundance (see e.g. [122])

$$\omega_{\rm DM} \equiv \Omega_{\rm DM} h^2 = g\chi \frac{m_{\rm NRP}[\rm eV]}{94\ \rm eV}. \tag{2.22}$$

Therefore we can rewrite maximal value of the primordial phase-space density (2.22) as

$$f_{max,\rm NRP} = \frac{94\omega_{\rm DM}}{2(2\pi\hbar)^3}\frac{m_{\rm NRP}^3}{\rm eV^3}\,. \tag{2.23}$$

Notice, that unlike the Fermi-Dirac case, for the non-resonant production scenario f_{max} behaves as the *third* power of particle's mass.

In the presence of lepton asymmetry in primeval plasma the resonant production of sterile neutrinos becomes possible [78]. A possible lepton asymmetry, generated in the framework of the νMSM and spectra of sterile neutrino dark matter were recently computed in [87, 88]. Qualitatively, these spectra contain a "cold" (resonant) component and a "warm" one, produced through non-resonant oscillations, analogously to the non-resonant production scenario of [56]. The spectra as a whole become colder than in the non-resonant production case (see e.g. Fig. 6 in [88]). The maxima of primordial phase-space distributions for these spectra are higher (sometimes significantly) than for spectra, produced in the non-resonant production scenario (c.f. Fig. 5 in [88]). Therefore, in general mass bound for such a dark matter is expected to be weaker than that of the non-resonant production scenario. The exact form of these spectra can be computed only numerically. We used a number of spectra to check those which satisfy the bound (2.18) or TG bound (see Section 2.6).

Let us compare expression (2.17) with the original Tremaine-Gunn bound (maximum of the right hand side of Eq. (2.6)):

$$F_{\rm TG} = \frac{9}{8\pi^2\sqrt{2\pi}G_N\sigma r_c^2}\,. \tag{2.24}$$

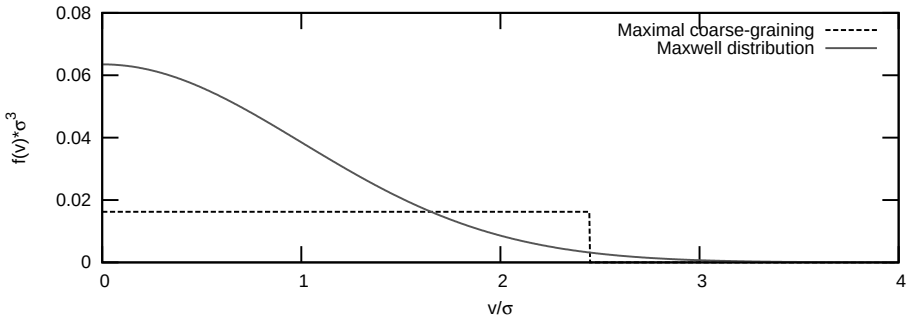

Figure 2.1: Comparison of velocity profiles assumed in [45] (grey solid line) and in this work (black dashed line).

The values of $\bar{F}$ is smaller than $F_{\rm TG}$ by

$$\frac{\bar{F}}{F_{\rm TG}} = \frac{\log 2\sqrt{\pi}}{6\sqrt{3}} \left(\frac{r_c}{r_h}\right)^2 \approx 0.118 \left(\frac{r_c}{r_h}\right)^2 , \qquad (2.25)$$

where r_c and r_h are the core radius of isothermal profile and the half-light radius, correspondingly. When comparing $\bar{F}$ and $F_{\rm TG}$ below, we take $r_h \simeq r_c$. Essentially, the difference between $\bar{F}$ and $F_{\rm TG}$ is due to the different assumed velocity distributions. While the Maxwell distribution was assumed in [45] (c.f. Eq. (2.5)), we assume constant velocity profile from escape velocity v_∞ down to $v = 0$ (as shown on the Fig. 2.1). The numerical factor in (2.25) is the ratio of areas under two velocity curves of Fig. 2.1. Translated into the mass bound, relation (2.25) means that for dark matter particles with distribution (2.4) one would obtain roughly 40% stronger mass bound by using the original Tremaine-Gunn bound, rather than $\bar{F}$ (and $\approx 60\%$ stronger mass bound for the case of the distribution (2.20)).

Let us compare our new bound with the one, based of [175, 176]. Following the definition (2.7), we express the measured value Q_f for a dSph through the observed quantities

$$Q = \frac{\bar{\rho}}{\eta^3 (3\sigma^2)^{3/2}} \approx 14.83 \frac{M_\odot}{\mathrm{pc}^3} \left(\frac{\mathrm{km}}{\mathrm{sec}}\right)^{-3} \left(\frac{\mathrm{km\,sec}^{-1}}{\sigma}\right) \left(\frac{1\,\mathrm{pc}}{r_h}\right)^2 \frac{1}{\eta^3} , \qquad (2.26)$$

where η is the scaling factor which accounts for the fact that the dark matter particles do not necessarily have the same velocity dispersion as the stars, r_h is the half-light radius, σ is the measured one-dimensional velocity dispersion of the stars and $\bar{\rho}$ is defined in (2.16). It was estimated in [176]

that $\eta \approx 1$. In Eq. (2.26) we used the same value of $\bar{\rho}$ as in Eq. (2.17). For the same dSph, Q_f is bigger than $\bar{F}$ (given by expression (2.17)) by a factor $8\pi\sqrt{2}/3 \approx 11.85\ldots$.

On the other hand, for any initial momentum distribution $f(p)$ we should compare Q_i, given by Eq. (2.8), with the $f^{(i)}_{max}$. For both types of distribution (2.4) and (2.20) the ratio of initial Q_i/f^i_{max} is given by

$$\frac{Q_i}{f^{(i)}_{max}} = \frac{4\pi\zeta^{5/2}(3)}{5\sqrt{15}\zeta^{3/2}(5)} \approx 0.973\ldots \tag{2.27}$$

As a result, a bound, based on the decrease of the average phase-space density Q is stronger than $\bar{F}$ bound from the same object by a factor:

$$\frac{f^{(i)}_{max}}{Q_i}\frac{Q_f}{\bar{F}} \approx 12.176\ldots \tag{2.28}$$

(where again we put $\eta = 1$). This leads to ≈ 1.87 times stronger bound on the $m_{\rm FD}$ and ≈ 2.3 times stronger bound for $m_{\rm NRP}$.

2.4 Analysis of measured values

In this Section we estimate phase-space density in different dark matter-dominated objects. We demonstrate that the dwarf spheroidal satellites of the Milky Way possess the highest phase-space density and thus provide the strongest limits on the mass of dark matter particles.

2.4.1 Galaxies

In this Section we study the restrictions on the mass of dark matter particles, coming from the analysis of the phase-space density of spiral galaxies. The distribution of dark matter is modeled based the analysis of the *rotational curves* — dependence of the circular rotational velocity of stars (optical data) and neutral hydrogen (radio data) around the galaxy centre as a function of distance (for mass modeling of the Milky Way, see e.g. [194, 195], for Andromeda galaxy – [11, 12]). Well outside the galactic bulge where the circular velocity curve flattens, the dark matter density can be found with the help of the following relation

$$\bar{\rho}_{gal} = \frac{3}{4\pi G_N}\frac{v_h^2(r)}{r^2}, \tag{2.29}$$

where $v_h(r)$ – part of the rotational velocity, contributed to dark matter [5] at distance r from the galaxy centre and is (approximately) constant. The velocity of dark matter particles in a compact halo does not exceed $v_\infty = \sqrt{2} v_h^{max}$. Here v_h^{max} is the maximum of the rotation curve, reached at some radius r_{max} before starting to decline. However, there are only few objects (classical dSphs) for which the value of v_h^{max} and r_{max} had been measured, see e.g. [196]). Therefore determination of these values provides the strongest uncertainty in the evaluation of the phase-space density of dark matter in spiral galaxies.

We write the phase-space density estimate as (see also (2.15))

$$\bar{F}_{gal} = \frac{3\bar{\rho}_{gal}}{4v_\infty^3} = \frac{9}{32\pi^2\sqrt{2}G_N v_h(r_{gal}) r_{gal}^2}, \tag{2.30}$$

where r_{gal} is the *inner* radius of the halo, some proxy for r_{max}. To be conservative we use r_{gal}, where the dark matter contribution is equal to contribution from barionic matter (the sum of bulge and disk components).

For the subsequent analysis we used two spiral galaxies with the best studied haloes – Milky Way and Andromeda galaxy. The velocity profiles for these galaxies are shown, e.g., in [194, 197]. The results for r_{gal} and $v_h(r_{gal})$, as well as the obtained bounds for $\bar{F}$ are shown in Table 2.1.

The average value of the lower mass bound from Table 2.1 implies $m_{\rm DEG} > 34$eV, $m_{\rm FD} > 40$eV. As we will see in Sec. 2.4.3 below, it is much weaker compared to bound obtained from dwarf spheroidal galaxies. Therefore, if the dSph dynamics (in contrast to dynamics of spiral galaxies) is *not* due to dark matter, the lower mass bound in the dark matter particles is ~ 40 eV, depending on the dark matter species.

2.4.2 Galaxy groups

The dark matter profiles in galaxy groups are obtained from the analysis of X-ray thermal emission distribution from tha hot gas halo. In this paper, we used the data from [198], where the distributions of dark matter, baryonic matter in galaxies and hot integralactic gas are derived. Similar to previous subsection, to take into account the uncertainties of dark matter and hot gas

[5] Note that this velocity is somewhat lower than the total rotational velocity of stars around the galaxy centre. This is due to the presence of two additional components – disk and buldge – formed by the luminous matter.

Profile (1)	Ref. (2)	r_{gal} kpc (3)	$v(r_{gal})$ km/sec (4)	$\bar{F}_{gal}$, $M_\odot\times$ pc^{-3} (km/sec)$^{-3}$ (5)	$m_{\rm DEG}$ keV (6)	$m_{\rm FD}$ keV (7)
MW, A1	[194]	3.0±0.6	150±10	3.45 $\times 10^{-9}$	0.043	0.051
M31, C1	[194]	3.8±0.8	180±10	1.79 $\times 10^{-9}$	0.036	0.043
M31a	[197]	6.0±1.2	140±10	0.93 $\times 10^{-9}$	0.031	0.037
M31b	[197]	6.5±1.3	140±10	0.79 $\times 10^{-9}$	0.030	0.035
M31c	[197]	6.0±1.2	150±10	0.86 $\times 10^{-9}$	0.030	0.036

Table 2.1: Parameters of selected spiral galaxies from [194, 197] (columns 1-5) and obtained lower mass bounds for different dark matter types (columns 6-7). $m_{\rm DEG}$ denotes the model-independent bound coming from Pauli principle (2.1), $m_{\rm FD}$ – model-dependent bound for dark matter particles with momentum distribution (2.4).

distribution we use the phase-space density values calculated in r_{gr}, where dark matter mass $M_{gr} = M(r_{gr})$ starts to dominate over the barionic mass. The maximal velocity of dark matter particles is estimated as

$$v_\infty = \sqrt{\frac{2G_N M_{gr}}{r_{gr}}}, \tag{2.31}$$

from what (using (2.15)) we obtain the conservative estimate of the maximal phase-space density value,

$$\bar{F}_{gr} = \frac{9}{32\sqrt{2}\pi^2 G_N^3/2M_{gr}^1/2r_{gr}^{3/2}.} \tag{2.32}$$

The results are presented in Table 2.2. The averaged values of the mass bound, derived from Table 2.2 are $m_{\rm DEG} > 24$ eV, $m_{\rm FD} > 29$ eV. Therefore, if the dSph dynamics, in contrast to dymamics of spiral galaxies and galaxy groups, is not due to dark matter, the lower bounds on the dark matter particle mass is $\sim$ 25-30 eV, depending on the dark matter model.

2.4.3 Dwarf spheroidal galaxies

Dwarf spheroidal galaxies (dSphs) are the compact (around $\sim$ 1 kpc) and gravitationally bound systems with low surface brightness and high velocity dispersion. To explain the latter, one needs to introduce the mass-to-luminosity value with is hundreds times more than the value observed in

Object (1)	Ref. (2)	M_{gr} $10^{10} M_\odot$ (3)	r_{gr} kpc (4)	$\bar{F}_{gr}$, $M_\odot \times$ pc^{-3} (km/sec)$^{-3}$ (5)	$m_{\rm DEG}$ keV (6)	$m_{\rm FD}$ keV (7)
Abell 262	[198]	6.5±0.7	6.5±1.7	5.34×10^{-10}	0.027	0.032
NGC 533	[198]	5.0±0.5	5.0±1.5	9.02×10^{-10}	0.031	0.037
MKW 4	[198]	25±3	12.0±3.6	1.08×10^{-10}	0.018	0.022
IC 1860	[198]	13±1	9.5±2.9	2.14×10^{-10}	0.021	0.026

Table 2.2: Parameters of chosen galaxy groups from [198] (columns 1-5) and obtained lower mass bounds for different dark matter types (columns 6-7). $m_{\rm DEG}$ denotes the model-independent bound coming from Pauli principle (2.1), $m_{\rm FD}$ – model-dependent bound for dark matter particles with momentum distribution (2.4).

usual galaxies (see, for example, [199]). The possible reason for such a huge velocity dispersion is the disturbance of the cental part of dSphs with the tidal forces of our Galaxy. However, the observable features of tidal disturbance – the so-called "tidal tails", formed from stars which is going out of dSph – were found in single dSphs (Sagitarius, Ursa Major II). Therefore, the most realistic model by the moment for a *majority* of dSphs is their domination with dark matter. As a result, it is assumed that the dSphs are the *most compact* objects dominated with dark matter.

Over the last several years, a number of very faint, very dense dSphs were detected [200–206]. To calculate the mass limits, we used the data from two papers [205, 206] in which the dark matter phase-space density was estimated. First of all, we should notice that although both of these papers provide the estimate of Q for each object, they use different prescriptions for computing this value.

In [205] the quantity Q is estimated inside the half-light radius r_h, using one-dimensional velocity dispersion σ of stars:

$$Q_{Gil} = \frac{\bar{\rho}}{\sigma^3} = \frac{3}{8\pi G_N r_h^2 \sigma} \ . \tag{2.33}$$

Compared to our definition (2.17) $\bar{F} = \frac{\log 2}{2\sqrt{6}\pi} Q_{Gil} \approx 0.045 Q_{Gil}$. Following [207] the authors of [206] define *central density*

$$\rho_0 = 166 \sigma^2 \eta^2 / r_c^2 \tag{2.34}$$

where $\eta \sim 1$ is a numerical parameter, characterizing plausible density pro-

Galaxy	r_h, Plummer	r_h, exponential
Coma Berenices	5.0'	5.9'
Canes Venatici II	3.0'	3.3'
Leo IV	3.3'	3.4'
Hercules	8.0'	8.4'

Table 2.3: Uncertainties of determination of half-light radius r_h for several dSphs.

files (for details see [206, 207]). They used ρ_0 to define the quantity:

$$Q_{SG} \equiv \frac{\rho_0}{\sigma^3} \,, \tag{2.35}$$

As a result for the same object Q_{SG} is by a factor of 14.60 greater than Q_{Gil}.

Using the available information about dSph galaxies (refs. [205, 206] and refs. therein), we calculate $\bar{F}$, trying also to estimate the errors. Several factors contribute to the errors of σ and r_h.

First of all, as σ is the dispersion of measured velocities, it has the statistical error (which can be quite large for the ultra-faint dSphs where the number of stars can be rather small ($\sim 10-100$, c.f. [206, Table 3]). However, the systematic error is much larger. The authors of [206] found the systematic error on their determination of velocity dispersion to be $2.2\,\mathrm{km/\,sec}$. We add this error in quadratures to the statistical errors, found in [206, Table 3]. The results are shown in the column number 4 in the Table 2.4.

The half-light radius r_h is a derived quantity and there are several contributions to its errors. First of all, the surface brightness profile is measured in angular units and their conversion to parsecs requires the knowledge of the distance towards the object. These distances are generally known with uncertainties of about 10% (see [199, 199, 200, 203, 208–217]). Another uncertainty comes from the method of determination of r_h. The surface brightness profile gets fit to various models to determine this quantity. For several dSphs: Coma Berenices, Canes Venatici II, Hercules and Leo IV authors used two different profiles (Plummer and exponential) for evaluating the annular half-light radius [200]. Their results are present in the Table 2.3. We use these results to estimate the systematic error on r_h to be 20% and use it for all the dSph, where r_h is quoted without errors. The results of determination r_h are shown in the 3rd column of the Table 2.4. The obtained values of $\bar{F}$ with corresponding errors are presented in the Table 2.4, column

5. We determined the errors on $\bar{F}$ by pushing the uncertainties in both σ and r_h so that the values of $\bar{F}$ is minimized (maximized).

2.5 Influence of aspherical shapes of dark matter halos

In this Section we analyze how the bound changes due to the deviation of a dark matter halo from a spherical shape. Such asphericity affects both the spatial volume V and the escape velocity v_∞. We consider the dSph as homogeneous ellipsoid with semi-axes a, b and c and assume the ellipticity of its 2D projection[6] $\epsilon \lesssim 0.5$. Because we observe only 2D projection of such an ellipsoid, there are two possibilities:

Prolate dSph: $c > b \simeq a$. We see the axes b and c, related to the "averaged" radius R via $b = R(1-\epsilon)^{1/2}, c = R(1-\epsilon)^{-1/2}$. The spatial volume V is therefore

$$V = \frac{4}{3}\pi abc \approx \frac{4}{3}\pi R^3(1-\epsilon)^{1/2} \approx \frac{4}{3}\pi R^3(1-0.5\epsilon). \tag{2.36}$$

The gravitational potential for $\epsilon \lesssim 0.5$ is dominated by monopole and quadrupole components,

$$\phi \approx \phi^{(0)} + \phi^{(2)}. \tag{2.37}$$

The maximal value of the potential occurs near the end of the minor semi-axis:

$$|\phi_{max}| \equiv \frac{v_\infty^2}{2} = \frac{G_N M}{a} - \frac{G_N D_{zz}}{4a^3}, \tag{2.38}$$

where $D_{zz} = \frac{2M(c^2-a^2)}{5}$ – the quadrupole moment of the system [218]. For $\epsilon \ll 1$ we then obtain

$$\frac{V v_\infty^3|_{prolate}}{V v_\infty^3|_{spherical}} \approx 1 + 0.05\epsilon, \tag{2.39}$$

which gives us the correction for $m_{\rm DEG}$ of smaller than 1% (for $\epsilon = 0.5$).

[6]Throughout this paper, we define the *ellipticity* ϵ in a way similar to that in [174] (see also [166]), i.e. $\epsilon \equiv 1 - b/a$, where a and b are the *semi-major* and *semi-minor* axis, respectively. Thus, the case of $\epsilon = 0.5$ corresponds to axis ratio 1:2.

Oblate dSph: $c \simeq b > a$. We observe the axes a and c, therefore the spatial volume V changes by $(1-\epsilon)^{-1/2} \approx 1 + 0.5\epsilon$. The maximum of the gravitational potential is then given by

$$|\phi_{max}| \approx \frac{G_N M}{a} + \frac{G_N D_{xx}}{2a^3} \approx \frac{G_N M}{R}(1 + 0.1\epsilon). \tag{2.40}$$

where D_{xx} is given by the same expression, as D_{zz} above. The maximal phase-space volume changes in the oblate case by $\approx 1 + 0.65\epsilon$, so the correction for $m_{\rm DEG}$ will constitute about 8% for $\epsilon \simeq 0.5$.

Thus, the departure from spherical symmetry for dark matter halos of dSphs changes the limit on $m_{\rm DEG}$ by less than $\lesssim 10\%$ for the case of axis ratio 1:2. This uncertainty is below several others, therefore, we will consider dSphs to be spherical in what follows.

dSph (1)	References (2)	r_h pc (3)	σ km/s (4)	$\bar{F}$ $M_\odot/(pc^3(km/s)^3)$ (5)	m_{DEG} keV/c^2 (6)	m_{FD} keV/c^2 (7)	m_{NRP} keV/c^2 (8)	$m_{NRP,TG}$ keV/c^2 (9)
dSphs from [205]								
Sextans	[199, 205]	630±170	6.6±2.3	$4.78^{+8.97}_{-2.58}\cdot10^{-7}$	$0.147^{+0.044}_{-0.026}$	$0.174^{+0.053}_{-0.031}$	$0.454^{+0.192}_{-0.104}$	$0.715^{+0.302}_{-0.163}$
Fornax	[199, 205]	400±103	10.5±2.7	$7.45^{+10.74}_{-3.70}\cdot10^{-7}$	$0.164^{+0.041}_{-0.026}$	$0.195^{+0.049}_{-0.031}$	$0.527^{+0.183}_{-0.108}$	$0.830^{+0.288}_{-0.170}$
Leo I	[199, 205]	330±106	8.8±2.4	$1.31^{+2.59}_{-0.72}\cdot10^{-6}$	$0.189^{+0.059}_{-0.034}$	$0.224^{+0.070}_{-0.041}$	$0.635^{+0.279}_{-0.148}$	$1.00^{+0.44}_{-0.23}$
UrsaMinor	[199, 205]	300±74	9.3±2.8	$1.49^{+2.27}_{-0.76}\cdot10^{-6}$	$0.195^{+0.051}_{-0.031}$	$0.232^{+0.060}_{-0.037}$	$0.665^{+0.240}_{-0.139}$	$1.05^{+0.38}_{-0.22}$
Carina	[199, 205]	290±72	6.8±1.6	$2.19^{+2.87}_{-1.05}\cdot10^{-6}$	$0.215^{+0.050}_{-0.032}$	$0.255^{+0.060}_{-0.039}$	$0.755^{+0.243}_{-0.148}$	$1.19^{+0.38}_{-0.23}$
Draco	[166, 205]	221±16	9.5±1.6	$2.70^{+1.07}_{-0.69}\cdot10^{-6}$	$0.226^{+0.020}_{-0.016}$	$0.269^{+0.023}_{-0.019}$	$0.809^{+0.095}_{-0.076}$	$1.27^{+0.15}_{-0.12}$
Bootes	[199, 204, 219]	246±28	$6.5^{+2.1}_{-1.3}$	$3.18^{+1.88}_{-1.24}\cdot10^{-6}$	$0.236^{+0.029}_{-0.027}$	$0.280^{+0.035}_{-0.033}$	$0.855^{+0.143}_{-0.130}$	$1.35^{+0.23}_{-0.20}$
Sculptor	[199, 205]	160±40	10.1±0.3	$4.99^{+3.62}_{-1.98}\cdot10^{-6}$	$0.264^{+0.038}_{-0.031}$	$0.314^{+0.046}_{-0.037}$	$0.993^{+0.198}_{-0.154}$	$1.56^{+0.312}_{-0.243}$
Leo II	[199, 205]	185±48	6.8±0.7	$5.38^{+5.55}_{-2.30}\cdot10^{-6}$	$0.269^{+0.052}_{-0.035}$	$0.319^{+0.062}_{-0.042}$	$1.02^{+0.27}_{-0.17}$	$1.60^{+0.43}_{-0.27}$
dSphs from [206]								
Canes Venatici I	[166, 206]	564±36	7.6±2.2	$5.17^{+3.46}_{-1.63}\cdot10^{-7}$	$0.150^{+0.020}_{-0.013}$	$0.178^{+0.024}_{-0.016}$	$0.467^{+0.087}_{-0.055}$	$0.735^{+0.137}_{-0.087}$
Ursa Major I	[166, 206]	318^{+50}_{-39}	7.6±2.4	$1.63^{+1.46}_{-0.70}\cdot10^{-6}$	$0.199^{+0.035}_{-0.026}$	$0.237^{+0.041}_{-0.031}$	$0.684^{+0.163}_{-0.118}$	$1.08^{+0.26}_{-0.19}$
Hercules	[166, 206]	330^{+75}_{-52}	5.1±2.4	$2.25^{+3.74}_{-1.28}\cdot10^{-6}$	$0.216^{+0.060}_{-0.041}$	$0.257^{+0.071}_{-0.049}$	$0.762^{+0.294}_{-0.187}$	$1.20^{+0.46}_{-0.29}$
Leo T	[166, 206]	178±39	7.5±2.7	$5.26^{+8.22}_{-2.66}\cdot10^{-6}$	$0.267^{+0.071}_{-0.043}$	$0.318^{+0.084}_{-0.051}$	$1.01^{+0.37}_{-0.21}$	$1.59^{+0.59}_{-0.33}$
Ursa Major II[7]	[166, 206]	140±25	6.7±2.6	$9.53^{+13.55}_{-4.59}\cdot10^{-6}$	$0.310^{+0.077}_{-0.047}$	$0.369^{+0.091}_{-0.056}$	$1.23^{+0.42}_{-0.24}$	$1.94^{+0.67}_{-0.38}$
Leo IV	[166, 206]	116^{+26}_{-34}	3.3±2.8	$2.82^{+34.39}_{-1.91}\cdot10^{-5}$	$0.406^{+0.368}_{-0.100}$	$0.483^{+0.438}_{-0.119}$	$1.77^{+2.41}_{-0.55}$	$2.79^{+3.80}_{-0.87}$
Coma Berenices	[166, 206]	77 ± 10	4.6±2.3	$4.59^{+7.53}_{-2.19}\cdot10^{-5}$	$0.459^{+0.126}_{-0.069}$	$0.546^{+0.150}_{-0.082}$	$2.08^{+0.80}_{-0.41}$	$3.28^{+1.25}_{-0.64}$
Canes Venatici II	[166, 206]	74^{+14}_{-10}	4.6±2.4	$4.97^{+8.92}_{-2.66}\cdot10^{-5}$	$0.468^{+0.137}_{-0.082}$	$0.557^{+0.163}_{-0.097}$	$2.14^{+0.87}_{-0.48}$	$3.36^{+1.38}_{-0.76}$

Table 2.4: Parameters for dSphs from [205, 206] (columns 1–5) and derived lower mass limits for various types of dark matter (columns 6–9). m_{DEG} refers to the limit from Pauli exclusion principle (2.1), m_{FD} is the limit for particles with the momentum distribution (2.4), m_{NRP} and $m_{NRP,TG}$ – for distribution (2.20). All results are quoted for $g = 2$ internal degrees of freedom. Results for non-resonant production scenario are for $\omega_{DM} = 0.105$ [220].

2.6 Results

Our main results are compiled into the Table 2.4 (columns 6–9). The **column 6** of Table 2.4 contains the bound on $m_{\rm DEG}$ (given by Eq. (2.1)) based on the Pauli exclusion principle. It is independent of the details of the evolution of the system, is not affected by the presence of baryons (see below) and holds for any fermionic dark matter. The **column 7** contains the mass bounds for the relativistically decoupled dark matter particles (primordial distribution (2.4)), obtained by combining Eqs.(2.17)–(2.19). **Columns 8** and **9** are discussed below, Section 2.6.1.

We quote all the mass bounds with the corresponding uncertainties, coming from those of in determination of σ and r_h (see Section 2.4). However, for any given object there can be unique reasons, violating the standard assumptions and therefore increasing the uncertainties. Therefore, although the strongest bounds in Table 2.4 come from the Canes Venatici II dSph, we decided to take a value which independently follows from several objects as a single number, characterizing our results (for a given type of dark matter). To this end we choose the value, obtained for Leo IV.[8] Thus, the mass bounds, quoted below are excluded from three dSphs: Leo IV, Canes Venatici II and Coma Berenices [9]. To summarize, we obtain the following model independent lower bound, applicable to *any type of fermionic dark matter*:

$$m_{\rm DEG} > 0.41\,{\rm keV}/c^2\,, \tag{2.41}$$

If instead we assume that dark matter in the form of "*relativistic thermal relics*" with the Fermi-Dirac distribution, the bound becomes

$$m_{\rm FD} > 0.48\,{\rm keV}/c^2\,, \tag{2.42}$$

Notice, that we chose not to use the bounds, based on the "average phase-space density" Q [175, 176] (see discussion in the Section 2.2). However, as this bound is widely used in the literature, we quote analogs of lower

[8]Notice, that the numbers for Leo IV essentially coincide with the mass limits from Canes Venatici II and Coma Berenices if all uncertainties in these dSphs are pushed to *minimize* the mass bound.

[9]It is possible that Coma Berenices is undergoing tidal disruption (like another ultra-faint dSph, Ursa Major II , closely resembling Coma Berenices) [206]. However, unlike Ursa Major II (or the best known example of tidally disrupted dSph, Sagittarius), there are no known tidal streams near the position of Coma Berenices and the evidence in favor of tidal disruption are quite moderate (c.f. discussion in Sec. 3.6 of [206]).

limits (2.42) and (2.44) based on inequality (2.9) (which we denote $m_{\rm FD,HD}$ and $m_{\rm NRP,HD}$ correspondingly):

$$\begin{aligned} m_{\rm FD,HD} &= 0.9\,{\rm keV}/c^2\ , \\ m_{\rm NRP,HD} &= 4.0\,{\rm keV}/c^2\ . \end{aligned} \tag{2.43}$$

For details see Appendix 8.2.2.

2.6.1 Implication for sterile neutrino dark matter

In this Section we consider implications of our results for sterile neutrino dark matter. For sterile neutrinos, produced through non-resonant mixing with the active neutrinos ("*NRP production*" [56, 79, 81]). Combining Eqs. (2.17), (2.18) and (2.23) one obtains the result for the case of dark matter with primordial velocity distribution (2.20), quoted in the **column 8**. Both bounds in columns 7 and 8 conservatively assume maximally coarse-grained distribution function (see Section 2.3). In instead of the maximal coarse-graining, one assumes the isothermal distribution in the final state (c.f. Fig. 2.1), one arrives to the original Tremaine-Gunn bound, shown in the **9th column**. It is obtained by comparing the expressions (2.21) with (2.24).[10] We denote the corresponding mass bound by $m_{\rm NRP,TG}$.

$$m_{\rm NRP} > 1.77\,{\rm keV}/c^2\ , \tag{2.44}$$

and

$$m_{\rm NRP,TG} > 2.79\,{\rm keV}/c^2\ . \tag{2.45}$$

We can compare lower bounds (2.44)–(2.45) with the upper ones, coming from astrophysical (X-ray) constraints on the possible flux from sterile neutrino dark matter decay [221–231]. Taking central value (2.44) and comparing it with the X-ray constraints, one sees that there exists a narrow window of parameters for which 100% of dark matter can be made from the non-resonant produced sterile neutrino (c.f. Fig. 2.2). Less conservative bound (2.45), based on [45] (marked by the dark orange double-dotted vertical line on the Fig. 2.2) almost completely closes this window. Notice, that these bounds are comparable with the lower mass limit $m_{\rm NRP} > 5.6\,{\rm keV}/c^2$, coming from the Ly-$\alpha$ forest analysis of [126].

[10] The value of r_c is not currently known for several new, faint dSphs, from which we obtain the best limits on dark matter mass. Therefore, to calculate the Tremaine-Gunn limit in Table 2.4, we use the conservative estimate $r_c \approx r_h$ (see comment after Eq.(2.25)).

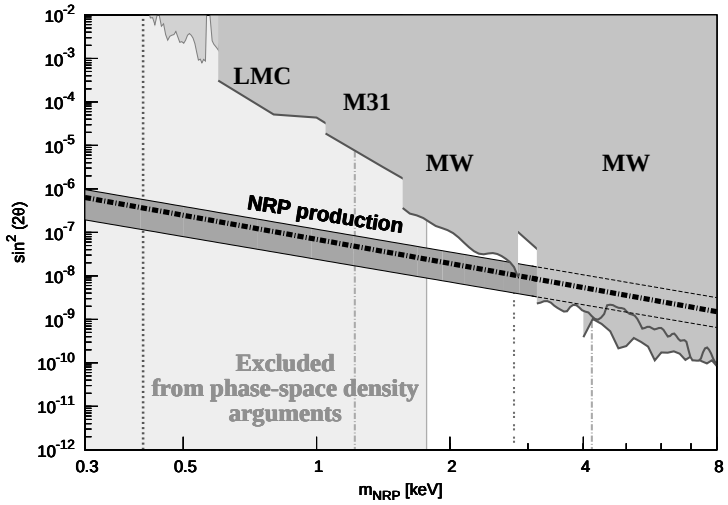

Figure 2.2: Restrictions on parameters of sterile neutrino (mass and mixing $\sin^2(2\theta)$ between sterile and active neutrinos) from X-rays ([223, 228–231]) and phase-space density considerations (this Chapter; see also [46]). Our analysis excludes the shaded region to the left of the vertical line (2.44). Two dashed-dotted vertical lines mark the systematic uncertainties of this bound. The dotted line on the left marks the bound (2.41) based on the Pauli exclusion principle. The double-dotted dark orange line marks the bound (2.45). The black dashed-dotted line is the *non-resonant production production curve* (i.e. pairs of $m_{\rm NRP}$ and θ that lead to the correct dark matter abundance) [81]. The gray region marked "NRP production" accounts for possible uncertainties in the abundance computations within non-resonant production scenario (see [81, 86] for details).

We also performed the analysis for sterile neutrinos, produced in the presence of lepton asymmetry (resonant production mechanism) [78, 87, 88]. This mechanism is more efficient than the non-resonant production scenario and allows us to achieve the required dark matter abundance for weaker mixings (c.f. Fig. 4 in [88]). This lifts the upper bound on the dark matter particle mass in resonant production scenario to $\sim 50 \ \ \mathrm{keV}/c^2$. To estimate the lower mass bound at this scenario, we have analyzed a number of available spectra (mass range $1 - 20\,\mathrm{keV}/c^2$, asymmetries $(2 - 700) \times 10^{-6}$ (see [87, 88] for the definition of asymmetry). The result are collected on the Fig. 2.3. One can see that based on $\bar{F}$, the $M_{\rm RP} = 1\,\mathrm{keV}/c^2$ is allowed for

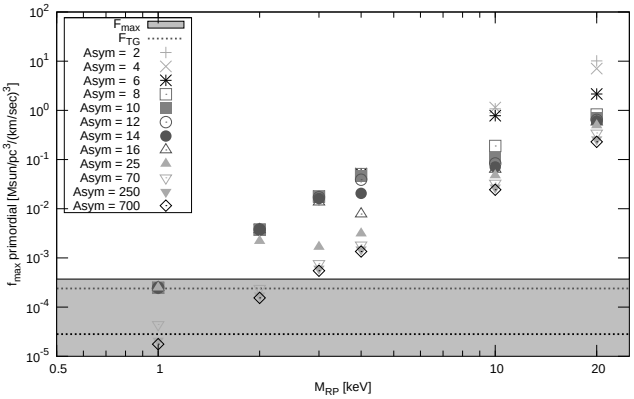

Figure 2.3: Restrictions on resonantly produced sterile neutrinos. Primordial f_{max} is computed numerically based on the spectra from [87, 88]. Different symbols parametrize different lepton asymmetries for a given mass (see definition of lepton asymmetry in [87, 88]). Grey shaded region is bounded by the maximal and minimal values of $\bar{F}$ for Leo IV (from Table 2.4, column 5). Horizontal dotted lines represent central value for $\bar{F}$ (lower) and $F_{\rm TG}$ (upper) for Leo IV. The dark matter spectrum is ruled out if the point falls into the shaded region (below the dotted line).

lepton asymmetries $L \gtrsim 10^{-4}$ and higher masses $M_{\rm RP} \geq 2\,\mathrm{keV}/c^2$ are allowed for all available asymmetries. Based on the original Tremaine-Gunn bound, $M_{\rm RP} = 2\,\mathrm{keV}/c^2$ is also allowed for sufficiently high ($L \gtrsim 10^{-4}$) lepton asymmetries. Thus, resonantly produced sterile neutrinos remain a viable dark matter candidate (see Fig. 2.4).

Finally, we would like to comment on the mechanism of production of sterile neutrinos from decay of massive scalar field, for example the inflaton [232] (for other models see [233–236]). The primordial phase-space distribution function for this case was computed e.g. in [232, 234, 236, 237]. Maximal value of phase-space density for this distribution is that of degenerate Fermi gas. Notice that the distribution functions in [232, 234, 236] $f(p)$ is formally unbounded for small momenta: $f(p) \sim p^{-1/2}$. From this one can easily find that the fraction of particles, having maximal phase-space density, is $\sim 10^{-8}$. As only this small fraction of all particles has maximal phase-space density, we expect the mass bound in this case to be stronger than (2.41).

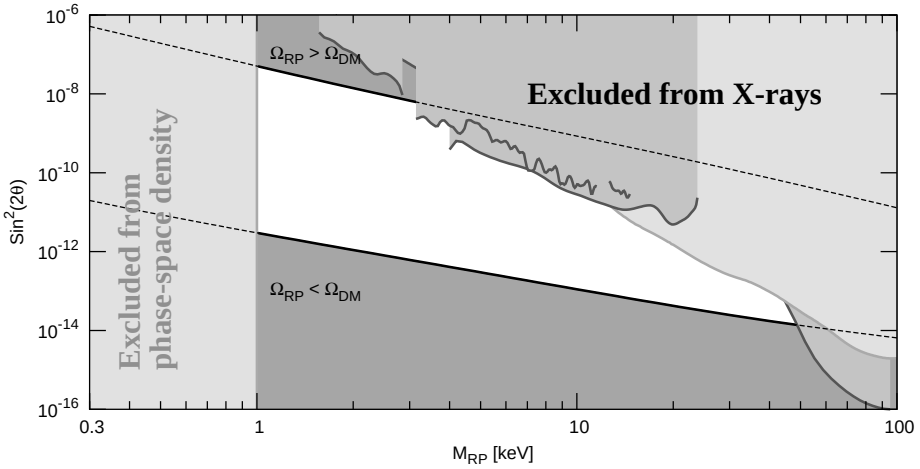

Figure 2.4: Allowed window of parameters for sterile neutrinos produced via resonant oscillations (white unshaded strip between two black lines). Two bounding black lines are obtained for non-resonant (upper line, lepton asymmetry $= 0$) and resonant production with the maximal lepton asymmetry, attainable in the νMSM [87, 88] (lower line). The grey regions in the upper right corner represent X-ray bounds [223, 228, 230, 231]. Region below $1\ \mathrm{keV}$ is ruled out from the phase-space density arguments (this work).

2.6.2 Influence of baryons

It should be noticed that our bounds (2.42)–(2.45) are valid under the assumption that the influence of the baryons does not result in the *increase* of the phase-space density in the course of structure formation. If this assumption does not hold, only the bound (2.41) remains intact. We discuss the robustness of this assumption below.

Although dark matter consists of the non-interacting particles, the remaining part of the galaxy – the baryons – interact with one another and dissipate their energy, finally concentrating towards the center. The baryons, which are condensed in the center, influence the shape of dark matter halo gravitationally, increasing the central dark matter density [238, 239]. The opposite effect is the energy feedback from SNae, galactic winds and reionization, which creates the strong outflow, significantly decreasing the mass of the gas and thereby affecting the dark matter halo shape. Such a

feedback is thought to be responsible to the formation of dwarf spheroidals from gas-rich dwarf spiral/irregular galaxies [240–244]. Clearly both gas condensation and feedback strongly influence the central phase-space density of dark matter [245], and in principle can lead to the violation of the inequality (2.3). Numerical studies of galaxy mergers show that baryons can lead to the increase of the phase-space density during the merger (see e.g. [246]). However, the method used in this work – coarse-graining of the phase-space density over a large phase-space region – reduces the influence of baryons. Indeed, we take the spatial averaging over the radius $R \sim r_h$, which includes external part of the system, where the amount of baryons is small. Additional studies are necessary to estimate effects of baryons and make our bounds more robust. We plan to address these issues elsewhere.

In the presence of lepton asymmetry, the resonant production of sterile neutrino dark matter takes place [78]. This mechanism is more efficient [78, 87, 88] than the non-resonant production scenario and allows to achieve required dark matter abundance for weaker mixings (c.f. Fig. 4 in [88]). This lifts the upper bound on the dark matter particle mass in this scenario up to $\sim 50\mathrm{keV}/c^2$. At the same time, for the same mass the primordial velocity distribution of resonant produced sterile neutrino dark matter is colder than in non-resonant production case. This f_{max} is as much as the order of magnitude bigger than (2.21) (c.f. [88]). This brings down by a factor ~ 2 the analog of the mass bound (2.44). Analyzing available spectra for a range of lepton asymmetries, we see that models with $m_{\mathrm{RP}} \gtrsim 1\ \mathrm{keV}/c^2$ are allowed. Thus, there is a large open "window" of allowed dark matter masses (c.f. Fig. 2.4). However, as the dependence of the velocity spectrum on the lepton assymetry is not monotonic, to obtain the exact shape of the lower bound on the mass at given mixing angle more work is needed. Nevertheless, our results show that the sterile neutrinos, produced in the presence of lepton asymmetry, are viable dark matter candidates, allowed by all current bounds.